Alignment of Irregular Grains by Mechanical Torques

Thiem Hoang ^{1,2} , Jungyeon Cho³ , and A. Lazarian ⁴

Korea Astronomy and Space Science Institute, Daejeon 34055, Korea; thiemhoang@kasi.re.kr

Korea University of Science and Technology, Daejeon, 34113, Korea

Department of Astronomy and Space Science, Chungnam National University, Daejeon, Korea

Astronomy Department, University of Wisconsin, Madison, WI 53706, USA

Received 2017 April 5; revised 2017 November 7; accepted 2017 November 29; published 2018 January 15

Abstract

We study the alignment of irregular dust grains by mechanical torques due to the drift of grains through the ambient gas. We first calculate mechanical alignment torques (MATs) resulting from specular reflection of gas atoms for seven irregular shapes: one shape of mirror symmetry, three highly irregular shapes (HIS), and three weakly irregular shapes (WIS). We find that the grain with mirror symmetry experiences negligible MATs due to its mirror-symmetry geometry. Three HIS can produce strong MATs, which exhibit some generic properties as radiative torques (RATs), while three WIS produce less efficient MATs. We then study grain alignment by MATs for the different angles between the drift velocity and the ambient magnetic field, for paramagnetic and superparamagnetic grains assuming efficient internal relaxation. We find that for HIS grains, MATs can align subsonically drifting grains in the same way as RATs, with low-J and high-J attractors. For supersonic drift, MATs can align grains with low-J and high-J attractors, analogous to RAT alignment by anisotropic radiation. We also show that the joint action of MATs and magnetic torques in grains with iron inclusions can lead to perfect MAT alignment. Our results point out the potential importance of MAT alignment for HIS grains predicted by the analytical model of Lazarian & Hoang, although more theoretical and observational studies are required due to uncertainty in the shape of interstellar grains. We outline astrophysical environments where MAT alignment is potentially important.

Key words: dust, extinction - magnetic fields - polarization - protoplanetary disks

1. Introduction

Interstellar dust is an intrinsic component of the interstellar medium and plays an important role in many astrophysical processes, including gas heating and cooling, and the formation of planets and stars. Observations of starlight polarization reveal that dust grains are non-spherical and aligned with the interstellar magnetic field (Hall 1949; Hiltner 1949). The alignment of interstellar grains allows us to trace the topology and to measure the strength of interstellar magnetic field through starlight polarization (Davis 1951; Chandrasekhar & Fermi 1953) and polarized thermal dust emission (Hildebrand 1988), in various astrophysical environments. Moreover, polarized thermal emission from aligned grains is a significant Galactic foreground contaminating cosmic microwave background (CMB) radiation, which is considered the most critical challenge to the quest of CMB B-modes as demonstrated by the joint BICEP2/Keck and Planck data analysis (Ade et al. 2015).

After more than 65 years since the discovery of starlight polarization (Hall 1949; Hiltner 1949), the problem of grain alignment of dust grains might be solved eventually (see latest reviews by Andersson et al. 2015 and Lazarian et al. 2015). The radiative torque (RAT) alignment (Dolginov & Mitrofanov 1976) is established as a dominant mechanism (Andersson et al. 2015; Lazarian et al. 2015). This mechanism relies on an anisotropic radiation source to spin-up (Draine & Weingartner 1996; hereafter DW96) and align irregular grains (Draine & Weingartner 1997; hereafter DW97; Lazarian & Hoang 2007a; Hoang & Lazarian 2008), and thus it is valuable for not very dense environments (Cho & Lazarian 2005; Whittet et al. 2008; Hoang & Lazarian 2014). In very dense regions, such as the shielded regions of protoplanetary disks, the alignment of classical grains is lost due to low radiation intensity (Cho & Lazarian 2007;

Hoang & Lazarian 2014).⁵ Powerful observation capabilities in the era of submillimeter/millimeter polarization (e.g., ALMA, JCMT) allow us to look into extremely dense regions where little radiation but active gas dynamics are present, such as protoplanetary disks. Therefore, it is of great importance to reexamine the alignment by non-radiative mechanisms, such as the mechanical one.

Mechanical alignment was pioneered by Gold (1952a, 1952b) in which random collisions with gas atoms stochastically increase the grain rotational energy, leading to the final alignment state with the long grain axis parallel to the gas flow. It was then elaborated by other researchers (e.g., Purcell 1969; Purcell & Spitzer 1971; Dolginov & Mitrofanov 1976; Lazarian 1994; Roberge et al. 1995). While the original mechanism could deal with thermally rotating grains only, two modifications of the mechanism that were introduced in Lazarian (1995a) and elaborated on later in Lazarian & Efroimsky (1996) enabled the alignment of grains rotating at much higher rates. The latter were introduced to the field by Purcell (1979), where the limitations on the size for suprathermally rotating grains were discussed).

The main shortcoming of the classical mechanical mechanism was that it required supersonic gas-dust drift to get any appreciable degree of alignment (see Purcell 1969). Although subsequent studies indicated that such grain drift can be produced by ambipolar diffusion in star-forming clouds (Roberge & Hanany 1990; Roberge et al. 1995) or interactions of charged grains with magnetohydrodynamic (MHD) turbulence (Lazarian 1994; Lazarian & Yan 2002; Yan et al. 2004; Hoang et al. 2012), the degree of alignment achievable for the

Very large grains can still be aligned by radiative torques induced by long-wavelength photons (Tazaki et al. 2017).

Mach number of the order of unity (typical conditions of the ISM) is insufficient to explain observations (see estimates in Lazarian 1997).

An alternative process based on the interaction of a gaseous flow with a *helical* grain was considered in Lazarian & Hoang (2007b; henceforth LH07b). The authors extended their analytical model of RAT alignment to include the anisotropic gas flow instead of a photon flux. LH07b found that the gas flow can produce strong regular mechanical torques when interacting with the helical grain. Those torques can align grains up to degrees from 30% to 100% even for *subsonic* gaseous flows (subsonic grain drift). In comparison, elaborate calculations in Lazarian (1997) show that the alignment in Gold's (1952b) original process does not exceed 20% for realistically flattened grains. Another mechanical alignment process, namely the cross-section mechanism (Lazarian 1995a; Lazarian 1997;) does not produce a high degree of alignment either.

The conclusions in LH07b have recently been supported by Das & Weingartner (2016) who numerically computed mechanical alignment torques (MATs) for 13 shapes built from Gaussian random spheres. In the absence of paramagnetic relaxation, they found that MAT alignment in the subsonic regime varies with the grain shapes (i.e., more efficient alignment for shapes with stronger MATs). Nevertheless, their results for MAT alignment of supersonic grains are consistent with the theoretical predictions in LH07b. To understand why MATs substantially vary with the grain shape (compare to radiative torques), in this paper, we will first conduct an analytical estimate of MATs for an irregular shape comprising many facets of random orientation and compare with the MAT of a helical grain from LH07b. Then we will calculate the torques for several irregular shapes that exhibit a much different degree of irregularity (see Section 3). Moreover, since we are interested in the analog of RATs and MATs, we will compute MATs of two irregular shapes chosen by DW97 that are found to produce strong RATs. Furthermore, to achieve a better understanding of MAT alignment for realistic conditions, we will study MAT alignment for the different drifting direction of grains with the ambient gas, in the presence of magnetic relaxation, for both ordinary paramagnetic grains and grains with iron inclusions. Note that the effect of magnetic relaxation was ignored in Das & Weingartner (2016).

We note that the incorporation of iron clusters into big grains plays an important role in the RAT alignment paradigm, which can produce universal high-*J* attractors (Lazarian & Hoang 2008). Interestingly, a recent experiment by Kimura et al. (2017) reveals that pure iron grains are rare due to low sticking probability, suggesting that iron is more likely present in dust grains as inclusions/compounds. Hoang & Lazarian (2016) carried out extensive simulations on the alignment of RATs for grains with iron inclusions and found that grains can perfectly be aligned with a moderate fraction (above 10%) of iron abundance in the form of nanoparticles. Thus, a similar effect should be applicable for MAT alignment.

The structure of the paper is as follows. In Section 2, we present analytical estimates of MATs from AMO and a simple irregular grain, finding a cancellation effect of MATs. Section 3 describes the irregular shapes used to compute mechanical torques. In Section 4, we present the model setup for calculations and the results of MATs. Section 5 is devoted to

studying in detail the alignment of grains by MATs for paramagnetic and superparamagnetic grains. A discussion and summary are shown in Sections 6 and 7, respectively.

2. Analytical Estimates of Mechanical Torques

2.1. MATs from an Analytical Model

Lazarian & Hoang (2007a; hereafter LH07a) first introduced a helical grain model built from an oblate spheroid attached to the massless mirror inclined with respect to the principal plane of the grain. They obtained an analytical description of RATs and made testable predictions of RAT alignment. Such a model is referred to as an analytical model (AMO).

LH07b used the LH07a's model but considered that atoms rather than photons impinge on the model grain. The corresponding calculation of torques for the supersonic case were identical to the calculation of the photon–grain interaction, but the calculations were also performed for the subsonic case where the effect of random thermal velocities of atoms is important. In both cases, substantial torques were reported. LH07b noticed that MATs for a realistic grain shape would experience reduction due to the *reflection efficiency factor E* and *helicity reduction factor D*. Nevertheless, the physics of the factor *D* is not yet quantified.

Following Equation (7) of LH07b, the MAT from AMO induced by a helical grain drifting through the gas of density $n_{\rm H}$ is given by

$$\Gamma_{\text{AMO}} = \frac{m_{\text{H}} n_{\text{H}} v_{\text{th}}^2 A l_1}{2} Q_{\text{AMO}}(s_d)$$

$$\sim 2 \times 10^{-27} a_{-5}^3 Q_{\text{AMO}}(s_d)$$

$$\times \left(\frac{n_{\text{H}}}{30 \text{ cm}^{-3}}\right) \left(\frac{T_{\text{gas}}}{100 \text{ K}}\right) \text{g cm}^2 \text{s}^{-2}, \tag{1}$$

where A is the area of the mirror and l_1 is the length from the center of mass to the mirror, $a_{-5} = a_{\rm eff}/10^{-5}\,{\rm cm}$ with $a_{\rm eff} = (3Al_1/4\pi)^{1/3}$ being the effective grain size, 6 and $Q_{\rm AMO}$ is the MAT efficiency (see Equation (6) in LH07b). For the above estimate, the thermal velocity $v_{\rm th} = (2kT_{\rm gas}/m_{\rm H})^{1/2}$ is evaluated for gas temperature $T_{\rm gas} = 100\,{\rm K}$ (see Table 8), and $Q_{\rm AMO}$ is roughly unity at $v_d = v_{\rm th}$ and increases with s_d .

The AMO appears to exhibit a highest degree of helicity because it has only one twisted facet exposed to the photon or gas flow. Any attempt adding one or more additional facets to the spheroid result in the decrease in grain helicity. Therefore, we expect the MAT from AMO is strongest.

2.2. MATs from a Simple Irregular Shape

Now, let us estimate the torque for a more realistic shape. We assume that the grain surface consists of N_{facet} facets with different orientations. When a stream of gas particles hit the grain surface, each facet acts as a mirror and provides a random contribution to the total torque.

The effective grain radius, $a_{\rm eff}$, is defined as the radius of the equivalent sphere of the same volume as the grain.

Here, irregularity is analogous to helicity.

The mechanical torque due to specular reflection by a facet is approximately given by

$$\delta\Gamma_{\rm MAT} \sim \left(n_{\rm H} \frac{4\pi a_{\rm eff}^2}{N_{\rm facet}} v_d\right) \gamma_r(m_{\rm H} v_d a_{\rm eff}),$$
 (2)

where γ_r is the reflection coefficient, and the grain surface area is $4\pi a_{\rm eff}^2$.

The net torque from N_{facet} facets can be calculated using the random walk formula:

$$\Gamma_{
m MAT} \sim \delta \Gamma_{
m MAT} \sqrt{\gamma_e N_{
m facet}} \ \sim 4 \pi \gamma_r \sqrt{\gamma_e} \, n_{
m H} m_{
m H} v_{
m gas}^2 rac{a_{
m eff}^3}{\sqrt{N_{
m facet}}}, \eqno(3)$$

where γ_e denotes the fraction of the grain surface area that is substantially exposed to the stream of particles.

By plugging the typical physical parameters into the above equation, one obtains

$$\Gamma_{\text{MAT}} \sim \frac{2 \times 10^{-28} a_{-5}^3}{\sqrt{N_{\text{facet}}}} \left(\frac{n_{\text{H}}}{30 \text{ cm}^{-3}}\right)$$

$$\times \left(\frac{T_{\text{gas}}}{100 \text{ K}}\right) \left(\frac{v_d}{v_{\text{th}}}\right)^2 \text{ g cm}^2 \text{ s}^{-2}, \tag{4}$$

where $\gamma_e = 1/6$ is adopted.

From Equations (4) and (1), we see that an arbitrary grain shape of $N_{\rm facet}$ facets has MATs reduced by a factor $\sqrt{N_{\rm facet}}$ from the AMO. For instance, a spheroidal or spherical shape has $N_{\rm facet} \gg 1$, leading to negligible MATs. The reduction of MATs from the AMO arises from averaging individual torques of random facets, which we term the *cancellation effect*. In the next section, we will compute MATs of grains made of finite facets.

3. Selective Irregular Grain Shapes

3.1. Highly and Weakly Irregular Shapes

An irregular grain shape is constructed by assembling N_{block} cubic blocks of unit volume. Our strategy to create an irregular shape is first to assembly a number of cubic blocks on a plane, the so-called *principal plane*. Then, we add a few blocks above and below the principal plane. Shape 1 is built from 5×3 blocks in the principal plane, 4 blocks above and 4 blocks below the principal plane. Shape 2 is made by a principal plane of 5×5 blocks and 16 blocks above and below the plane. Shapes 3–5 are slightly different in which there are three blocks on top of the principal plane. The principal plane of shape 3 is made by a layer of 5×5 blocks, shape 4 by two layers of 4×4 , and shape 5 is built from two layers of 5×5 . We also consider two shapes (denoted by shapes 6 and 7) built from 13 and 11 cubic blocks, similar to the shapes used for RAT calculations by DW96 and DW97. The grain shape is described by coordinates of the blocks and three principal axes \hat{a}_1 , \hat{a}_2 , \hat{a}_3 (see Tables 1-6).

Figure 1 shows the visualization of our selected irregular shapes. As seen, shape 1 exhibits mirror symmetry with respect to the principal axes \hat{a}_j . Shapes 3–5 are weakly irregular shapes (hereafter WIS), i.e., have a low degree of irregularities arising from the blocks on top of the principal plane, while shapes 2, 6, and 7 are highly irregular shapes (hereafter HIS), i.e., have a high degree of irregularities.

Table 1Coordinates of Blocks for Shapes 1 and 2

		Shape 2			Shape 1	
j	$\overline{x_j}$	y_j	z_j	x_j	y_j	z_j
1	1.0	1.0	1.0	1.0	1.0	1.0
2	2.0	1.0	1.0	2.0	1.0	1.0
3	3.0	1.0	1.0	3.0	1.0	1.0
4	4.0	1.0	1.0	1.0	2.0	1.0
5	5.0	1.0	1.0	2.0	2.0	1.0
6	1.0	2.0	1.0	3.0	2.0	1.0
7	2.0	2.0	1.0	1.0	3.0	1.0
8	3.0	2.0	1.0	2.0	3.0	1.0
9	4.0	2.0	1.0	3.0	3.0	1.0
10	5.0	2.0	1.0	1.0	4.0	1.0
11	1.0	3.0	1.0	2.0	4.0	1.0
12	2.0	3.0	1.0	3.0	4.0	1.0
13	3.0	3.0	1.0	1.0	5.0	1.0
14	4.0	3.0	1.0	2.0	5.0	1.0
15	5.0	3.0	1.0	3.0	5.0	1.0
16	1.0	4.0	1.0	2.0	2.0	2.0
17	2.0	4.0	1.0	2.0	3.0	2.0
18	3.0	4.0	1.0	2.0	4.0	2.0
19	4.0	4.0	1.0	2.0	2.0	0.0
20	5.0	4.0	1.0	2.0	3.0	0.0
21	1.0	5.0	1.0	2.0	4.0	0.0
22	2.0	5.0	1.0	2.0	3.0	3.0
23	3.0	5.0	1.0	2.0	3.0	-1.0
24	4.0	5.0	1.0			
25	5.0	5.0	1.0			
26	1.0	1.0	2.0			
27	1.0	1.0	0.0			
28	2.0	1.0	0.0			
29	4.0	1.0	2.0			
30	5.0	1.0	2.0			
31	5.0	1.0	0.0			
32	1.0	2.0	2.0			
33	5.0	2.0	0.0			
34	1.0	4.0	0.0			
35	5.0	4.0	2.0			
36	1.0	5.0	2.0			
37	1.0	5.0	0.0			
38	2.0	5.0	2.0		•••	
39	4.0	5.0	0.0			
40	5.0	5.0	2.0			
41	5.0	5.0	0.0			

The coordinates of constituent blocks for shapes 1–7 are shown in Tables 1–4. Table 5 shows the coordinates of the principal axes \hat{a}_j of seven shapes. For shapes 1 and 2, the principal axes are directed along the cube unit vectors. Shapes 3–5 have the principal axes almost aligned with the cube unit vectors. For this particular choice, when the grain drift is along the \hat{a}_1 axis, the torque for the rotation along \hat{a}_1 is expected to be negligible because incident atoms mostly hit a single symmetric surface.

The equivalent sphere radius of the grain in the code unit is given by

$$R_{\rm code} = \left(\frac{3N_{\rm block}}{4\pi}\right)^{1/3},\tag{5}$$

which can be converted to the physical unit $a_{\rm eff}$ via a scaling parameter $f_{cp}=a_{\rm eff}/R_{\rm code}$.

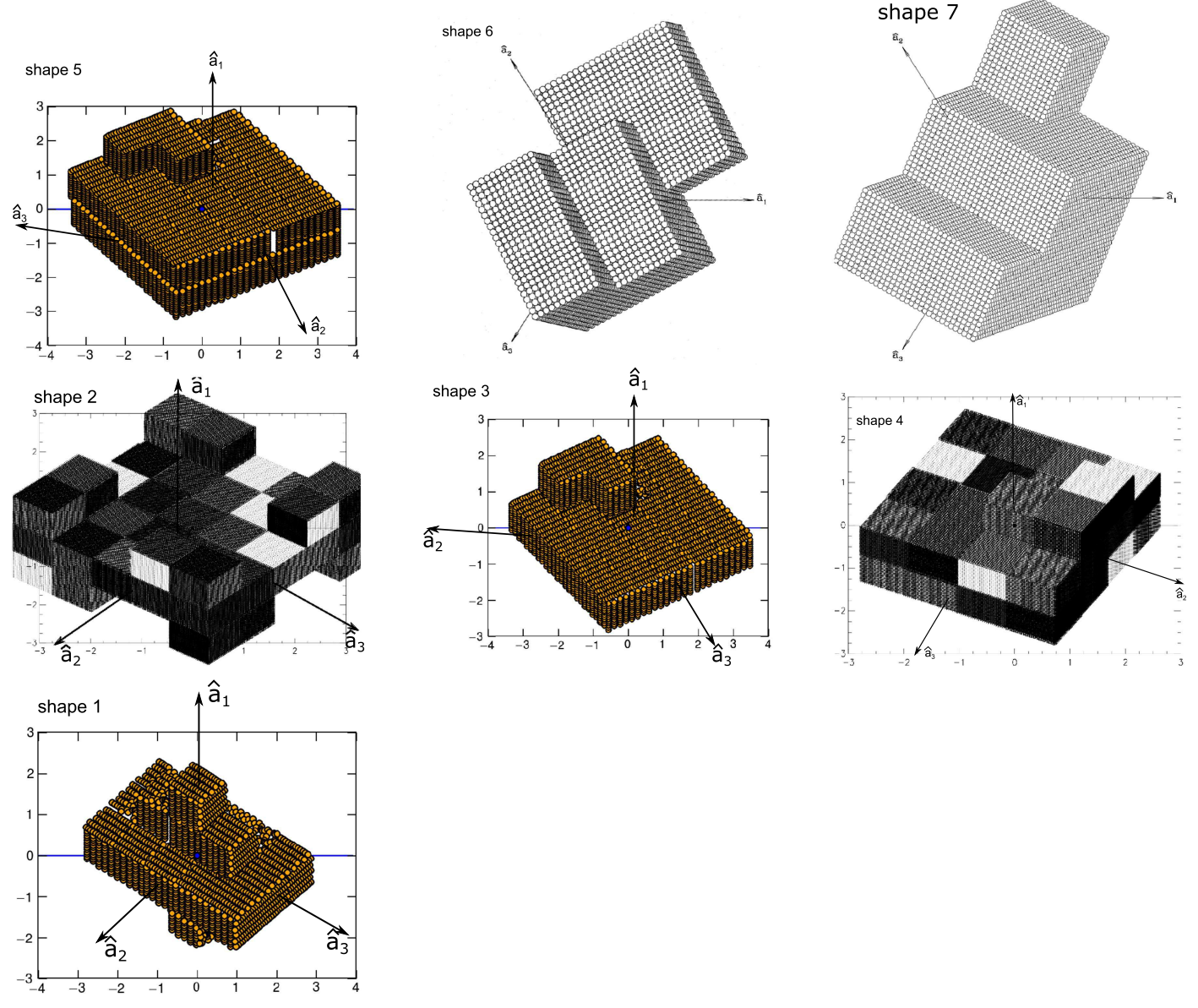


Figure 1. Visualization of seven irregular shapes constructed for our study of MAT alignment. Shapes 1–5 consist of a principal plane $\hat{a}_2\hat{a}_3$ and several blocks placed on the top/bottom of the plane. Shape 1 exhibits mirror symmetry.

The inertia moments along the principal axes are defined in terms of the equivalent sphere as follows:

$$I_j = \alpha_j \frac{8\pi \rho a_{\text{eff}}^5}{15},\tag{6}$$

where ρ is the mass density, α_j with j=1-3 are coefficients with $\alpha_j=1$ for spheres. Table 6 shows the coefficients α_j for the chosen irregular shapes.

4. Mechanical Torques: Numerical Method and Results

4.1. Model Setup and Coordinate Systems

Let us define a lab system \hat{e}_1 , \hat{e}_2 , \hat{e}_3 in which \hat{e}_1 is directed along the drift velocity v_d , $\hat{e}_2 \perp \hat{e}_1$, and $\hat{e}_3 = \hat{e}_1 \times \hat{e}_2$ (see Figure 2). The orientation of the grain in the lab frame is completely determined by the orientation of \hat{a}_1 and the rotation of the grain axes \hat{a}_2 around the \hat{a}_1 axis. The orientation of \hat{a}_1 is

defined by two angles Θ between \hat{a}_1 and v_d and the precession Φ . The rotation of the grain around \hat{a}_1 axis is determined by the angle β .

The impact position of an atom on a block is determined by the radius vector \mathbf{r} centered at the center of mass (CM) and its normal vector \mathbf{N} . Let $\hat{\mathbf{x}}$, $\hat{\mathbf{y}}$, $\hat{\mathbf{z}}$ be unit vectors along the three normal vectors of the cubic block. Each surface of the block is then divided into a grid of $N_1 \times N_1$ cells, with the regular resolution $dx = dy = 1/(N_1 - 1)$. The cell center of the mth block is determined by $\mathbf{r}_{c;m}$ for $m = 1 - N_{block}$. Thereby, the position of the cell ij of the surface m is given by

$$\mathbf{r}_{ij;m} = \mathbf{r}_{c;m} + id\mathbf{x} + jd\mathbf{y},\tag{7}$$

for i, j from $0 - N_1 - 1$, and dx = [dx, 0, 0], dy = [0, dy, 0]. The block's center radial vector is described by

$$\mathbf{r}_{c,m} = X_m \pm \frac{1}{2}\hat{\mathbf{x}} + \pm \frac{1}{2}\hat{\mathbf{y}} + \frac{1}{2}\hat{\mathbf{z}}.$$
 (8)

Table 2
Coordinates of Blocks for Shapes 3 and 4

	Shape 4			Shape 3			
j	$\overline{x_j}$	y_j	$\overline{z_j}$	$\overline{x_j}$	y_j	z_j	
1	1.0	1.0	1.0	1.0	1.0	1.0	
2	2.0	1.0	1.0	2.0	1.0	1.0	
3	3.0	1.0	1.0	3.0	1.0	1.0	
4	4.0	1.0	1.0	4.0	1.0	1.0	
5	1.0	2.0	1.0	5.0	1.0	1.0	
6	2.0	2.0	1.0	1.0	2.0	1.0	
7	3.0	2.0	1.0	2.0	2.0	1.0	
8	4.0	2.0	1.0	3.0	2.0	1.0	
9	1.0	3.0	1.0	4.0	2.0	1.0	
10	2.0	3.0	1.0	5.0	2.0	1.0	
11	3.0	3.0	1.0	1.0	3.0	1.0	
12	4.0	3.0	1.0	2.0	3.0	1.0	
13	1.0	4.0	1.0	3.0	3.0	1.0	
14	2.0	4.0	1.0	4.0	3.0	1.0	
15	3.0	4.0	1.0	5.0	3.0	1.0	
16	4.0	4.0	1.0	1.0	4.0	1.0	
17	1.0	1.0	0.0	2.0	4.0	1.0	
18	2.0	1.0	0.0	3.0	4.0	1.0	
19	3.0	1.0	0.0	4.0	4.0	1.0	
20	4.0	1.0	0.0	5.0	4.0	1.0	
21	1.0	2.0	0.0	1.0	5.0	1.0	
22	2.0	2.0	0.0	2.0	5.0	1.0	
23	3.0	2.0	0.0	3.0	5.0	1.0	
24	4.0	2.0	0.0	4.0	5.0	1.0	
25	1.0	3.0	0.0	5.0	5.0	1.0	
26	2.0	3.0	0.0	1.0	2.0	2.0	
27	3.0	3.0	0.0	1.0	3.0	2.0	
28	4.0	3.0	0.0	2.0	3.0	2.0	
29	1.0	4.0	0.0			• • •	
30	2.0	4.0	0.0				
31	3.0	4.0	0.0				
32	4.0	4.0	0.0				
33	1.0	2.0	2.0				
34	1.0	3.0	2.0				
35	2.0	3.0	2.0				

4.2. Numerical Method

4.2.1. Single Scattering

For calculations, we assume the perfect reflection of gas atoms by the grain surface. The torque produced by the single scattering (i.e., reflection) of atoms on an element of surface area dA of cell ij on block m is given by

$$d\mathbf{\Gamma}_{ii:m} = [\mathbf{r}_{ii:m} \times \Delta \mathbf{P}] dAf(\mathbf{s} - \mathbf{s}_d) d^3 s, \qquad (9)$$

where $s = v/v_{th}$, $s_d = v_d/v_{th}$, and

$$f(s - s_d) = n_{\text{H}} v_{\text{th}}(s - s_d) . N_{ij;m} e^{-s^2},$$

for $(s - s_d) . N_{ii;m} < 0,$ (10)

is the flux of incoming atoms that can collide with the grain surface element determined by the normal unit vector $N_{ij:m}$.

The angular momentum element ΔP is antiparallel to the normal vector and given by

$$\Delta \mathbf{P} = -2m_{\rm H} \mathbf{N}_{ii;m} |\mathbf{v} - \mathbf{v}_d| \cos \gamma, \tag{11}$$

where $\cos \gamma = -(\mathbf{v} - \mathbf{v}_d) \cdot N_{ij,m}/|\mathbf{v} - \mathbf{v}_d|$. In the following, we disregard the minor effect of thermal collisions and set s = 0.

Table 3
Coordinates of Blocks for Shape 5

j	x_j	y_j	z_j	j	X_j	y_j	z_j		
1	1.0	1.0	1.0	28	3.0	1.0	0.0		
2	2.0	1.0	1.0	29	4.0	1.0	0.0		
3	3.0	1.0	1.0	30	5.0	1.0	0.0		
4	4.0	1.0	1.0	31	1.0	2.0	0.0		
5	5.0	1.0	1.0	32	2.0	2.0	0.0		
6	1.0	2.0	1.0	33	3.0	2.0	0.0		
7	2.0	2.0	1.0	34	4.0	2.0	0.0		
8	3.0	2.0	1.0	35	5.0	2.0	0.0		
9	4.0	2.0	1.0	36	1.0	3.0	0.0		
10	5.0	2.0	1.0	37	2.0	3.0	0.0		
11	1.0	3.0	1.0	38	3.0	3.0	0.0		
12	2.0	3.0	1.0	39	4.0	3.0	0.0		
13	3.0	3.0	1.0	40	5.0	3.0	0.0		
14	4.0	3.0	1.0	41	1.0	4.0	0.0		
15	5.0	3.0	1.0	42	2.0	4.0	0.0		
16	1.0	4.0	1.0	43	3.0	4.0	0.0		
17	2.0	4.0	1.0	44	4.0	4.0	0.0		
18	3.0	4.0	1.0	45	5.0	4.0	0.0		
19	4.0	4.0	1.0	46	1.0	5.0	0.0		
20	5.0	4.0	1.0	47	2.0	5.0	0.0		
21	1.0	5.0	1.0	48	3.0	5.0	0.0		
22	2.0	5.0	1.0	49	4.0	5.0	0.0		
23	3.0	5.0	1.0	50	5.0	5.0	0.0		
24	4.0	5.0	1.0	51	1.0	2.0	2.0		
25	5.0	5.0	1.0	52	1.0	3.0	2.0		
26	1.0	1.0	0.0	53	2.0	3.0	2.0		
27	2.0	1.0	0.0	• • •	• • •	• • •	•••		

Table 4Coordinates of Blocks for Shapes 6 and 7

	Shape 6			Shape 7			
j	$\overline{x_j}$	y_j	$\overline{z_j}$	$\overline{x_j}$	y_j	z_j	
1	0	1	0	0	0	0	
2	0	1	1	1	0	0	
3	0	2	0	0	1	0	
4	0	2	1	1	1	0	
5	1	1	0	0	0	1	
6	1	1	1	1	0	1	
7	1	2	0	0	1	1	
8	1	2	1	1	1	1	
9	0	0	1	2	0	0	
10	0	0	2	2	1	0	
11	0	1	2	0	0	2	
12	2	1	0				
13	2	2	0				

 Table 5

 Coordinates of the Principal Axes for the Different Shapes

Shape	\hat{a}_{l}	$\hat{\boldsymbol{a}}_2$	\hat{a}_3
1	(0, 0, 1)	(1, 0, 0)	(0, 1, 0)
2	(0, 0, 1)	(1, 0, 0)	(0, 1, 0)
3	(0.08, 0.02, 0.99)	(0.23, -0.97, -0.01)	(0.97, 0.23, -0.08)
4	(0.15, -0.02, 0.98)	(0.07, 0.99, 0.01)	(-0.99, 0.07, 0.15)
5	(0.08, 0.015, 0.99)	(0.23, -0.97, 0.004)	(0.97, 0.23, -0.079)
6	(0.45, 0.43, 0.78)	(0.67, -0.74, 0.03)	(0.59, 0.50, -0.62)
7	(0.22, 0.83, 0.49)	(0.57, -0.52, 0.63)	(0.79, 0.13, -0.59)

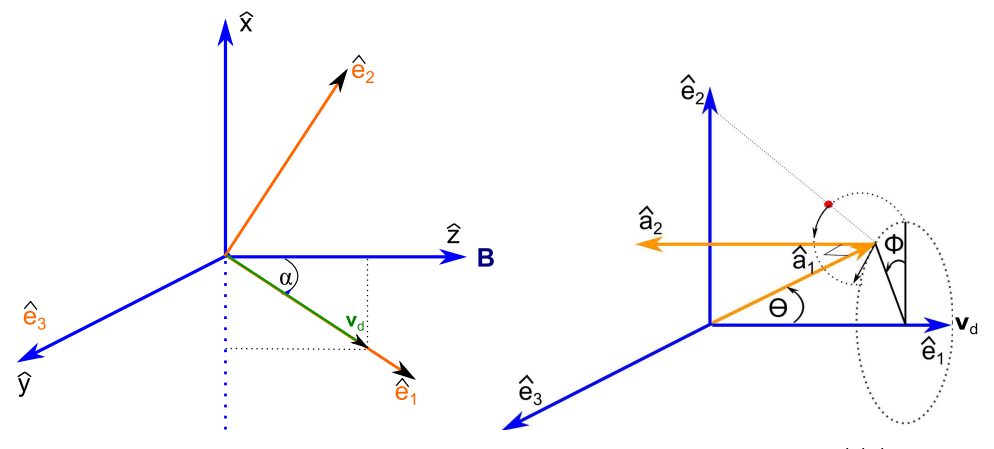


Figure 2. Coordinate systems used for calculations. Left panel: the direction of the grain drift in the fixed frame of reference $\hat{e}_1\hat{e}_2\hat{e}_3$ defined by the magnetic field B and $\hat{e}_1\|v_d$. The grain drift direction v_d lies in the plane $\hat{x}\hat{z}$ and makes an angle ψ with B. Right panel: orientation of grain principal axes \hat{a}_1 , \hat{a}_2 , \hat{a}_3 in the lab frame of reference.

Table 6 Coefficients α_i for the Different Shapes

Shape	$\alpha_{ m l}$	α_2	α_3
1	1.810	1.670	0.972
2	2.809	1.663	1.663
3	2.871	1.658	1.447
4	1.591	1.117	1.040
5	1.902	1.187	1.109
6	1.745	1.610	0.876
7	1.561	1.464	0.889

To find the total torque, Equation (9) is summed over all ij and m that are exposed to the gas flow:

$$\Gamma_{\text{MAT}} = \sum_{ij,m} d\Gamma_{ij,m},\tag{12}$$

where the interior cells of the grain are excluded.

The torque efficiency Q is defined as

$$\mathbf{\Gamma}_{\mathrm{MAT}} = \pi a_{\mathrm{eff}}^{2}(n_{\mathrm{H}} v_{\mathrm{th}})(m_{\mathrm{H}} v_{\mathrm{th}} a_{\mathrm{eff}}) \mathbf{Q}, \tag{13}$$

where Q has the torque components Q_{ai} with i = 1-3 and depends on s_d and the grain shape.

For convenience, the torque efficiency Q is first calculated in the coordinate system $\hat{x}\hat{y}\hat{z}$. Then, we evaluate the torque in the $\hat{a}_1\hat{a}_2\hat{a}_3$ frame as $Q_{ai}=Q.\hat{a}_i$ for i=1,2,3. Finally, we obtain the torque components Q_{ei} in the lab system $\hat{e}_1\hat{e}_2\hat{e}_3$ as follows:

$$Q_{ei} = \mathbf{Q}.\hat{\mathbf{e}}_i = \sum_{i=1}^{3} Q_{aj}\hat{\mathbf{a}}_j.\hat{\mathbf{e}}_i, \text{ for } i = 1, 2, 3,$$
 (14)

where the coordinate transformation from \hat{a}_j to \hat{e}_i is described in Hoang & Lazarian (2008).

4.2.2. Multiple Scattering

After reflection, gas atoms may continue to hit other facets of the grain, leading to multiple scattering. To calculate the torque by multiple scattering, we trace the trajectory of atoms after each reflection and calculate the torque contribution when the atom hits each surface.

Table 7
Model Parameters Used for MAT Calculations

Parameter	Meaning	Value
$n_{\rm H}({\rm cm}^{-3})$	Gas density	20
$T_{\rm gas}({ m K})$	Gas temperature	50
v_d (cm s ⁻¹)	Grain drift velocity	10 ⁵
$a_{\rm eff} (\mu {\rm m})$	Effective grain size	0.1

4.3. Results and Torque Properties

For our calculations, we consider $N_1 = N_2 = 50$ patches. Calculations are performed for 37 angles of Θ ($N_{\Theta} = 37$) and 36 angles of β ($N_{\beta} = 36$), having evenly divided grids. The torque efficiency is averaged over β due to fast rotation of the grain around \hat{a}_1 . Table 7 shows parameters adopted for our study.

Figure 3 shows the values of Q_{e1} and Q_{e2} for the seven different irregular shapes. Since the component Q_{e3} acts mainly to induce precession around the drift direction (LH07a), it is not shown here. The multiple scattering has a noticeable effect on the MAT, but the torques are essentially similar. From Figure 3, we find the following properties of MAT.

First, shape 1 has negligible torques, about 10⁴ orders of magnitude smaller than the other shapes. This naturally arises from the mirror symmetry of the grain shape combined with fast rotation around the axis of maximum moment of inertia.

Second, shapes 2, 6, and 7 (HIS) experience strong MATs. Moreover, MATs exhibit some basic properties as seen with RATs, having symmetric Q_{e1} and zero points of Q_{e2} at $\cos\Theta=\pm 1$. Note that shape 6 has right helicity, while 2 and shape 7 have negative helicity, as seen in their RATs (see LH07a).

Third, shapes 3–5 (WIS) have comparable torques, but an order of magnitude lower than shapes 2, 6, and 7. Such a comparable MAT efficiency is expected from the fact that the geometry of shapes 3–5 is only slightly different from each other (see Figure 1). Moreover, since these shapes contain only three blocks on top of the principal plane, the fraction of the gas flow that hits the flat principal plane is substantial, which results in the averaging out of the individual torques.

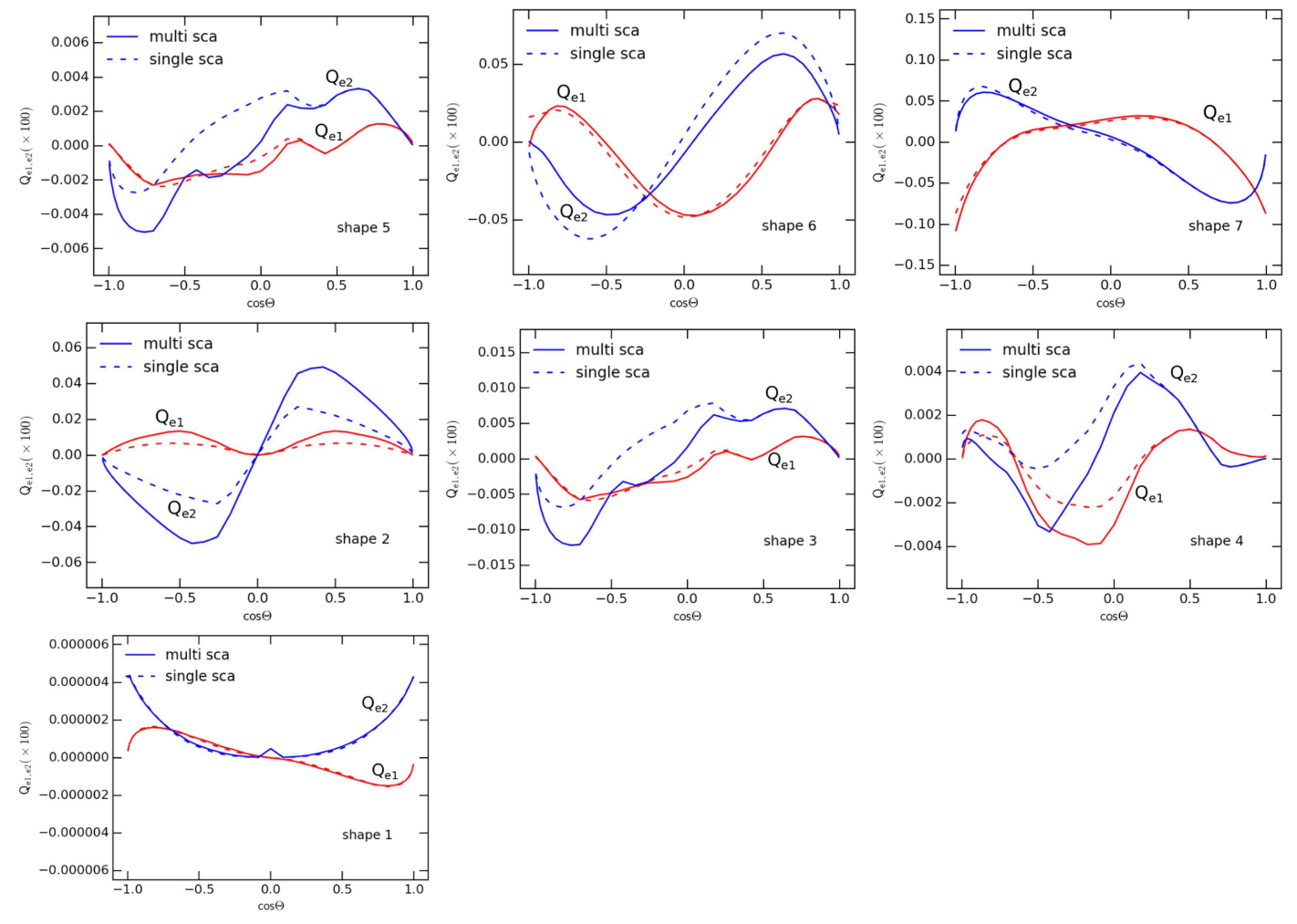


Figure 3. MAT components for the different shapes for the cases of single scattering (dashed lines) and multiple scattering (solid lines). Shape 1 has much lower MAT efficiency than other shapes due to its mirror-symmetry geometry, shapes 2, 6, and 7 have strong MATs with generic properties, and shapes 3–5 have weaker MATs. Multiple scattering slightly modifies the MAT.

Finally, the MAT efficiency of shapes 2–5 is negligibly small at $\cos\Theta=1$, i.e., when the direction of grain drift is parallel to the major axis \hat{a}_1 (see Figure 3 (panels (c)–(f)). This is due to the fact that for these chosen shapes, the principal axes \hat{a}_j are nearly along the basic unit vectors of the block (see Figure 1). Thus, when v_d is along \hat{a}_1 , gas atoms bombard a single symmetric surface of the grain at the right angle, producing negligible torques.

In summary, it is demonstrated that the degree of grain surface irregularity is an important factor of MAT efficiency.

5. Grain Alignment by Mechanical Torques

5.1. Dynamical Timescales

Sticking collisions of gas atoms to the dust grain surface followed by evaporation of thermalized molecules results in the loss of grain angular momentum. The rate of gas damping is given by

$$\Gamma_{\rm gas} = -\frac{J}{\tau_{\rm gas}},\tag{15}$$

where the τ_{gas} is the characteristic damping timescale for the rotation along the axis of major inertia \hat{a}_1 given by

$$\tau_{\rm gas} = \frac{\pi \alpha_1 \rho a_{\rm eff}}{3 \delta n_{\rm H} (2\pi m_{\rm H} k T_{\rm gas})^{1/2}},$$

$$\simeq 8.74 \times 10^4 \frac{\alpha_1}{\delta} \hat{\rho} a_{-5} \hat{T}^{1/2} \left(\frac{3000 \text{ cm}^{-3} \text{ K}}{n_{\rm H} T_{\rm gas}} \right) \text{ years}, \quad (16)$$

where $a_{-5} = a_{\rm eff}/10^{-5} \, {\rm cm}$, $\hat{\rho} = \rho/3 \, {\rm g \, cm^{-3}}$, $n_{\rm H}$ and $\hat{T} = T_{\rm gas}/100 \, {\rm K}$ are gas density and temperature, and δ is a parameter comparable to α_1 (DW97). For oblate spheroids with semimajor and minor axes a and b, we have $\alpha_1 = s^{-2/3}$ with s = b/a < 1.

Rotating paramagnetic grains experience paramagnetic relaxation, leading to the gradual alignment of grains with the magnetic field (Davis & Greenstein 1951). The characteristic time of such a paramagnetic relaxation is given by

$$\tau_{m} = \frac{I_{1}}{K(\omega)VB^{2}} = \frac{2\rho\alpha_{1}a_{\text{eff}}^{2}}{5K(\omega)B^{2}},$$

$$\simeq 1.5 \times 10^{6}\alpha_{1}\hat{\rho}a_{-5}^{2}\hat{B}^{-2}\hat{K}^{-1} \text{ years}, \tag{17}$$

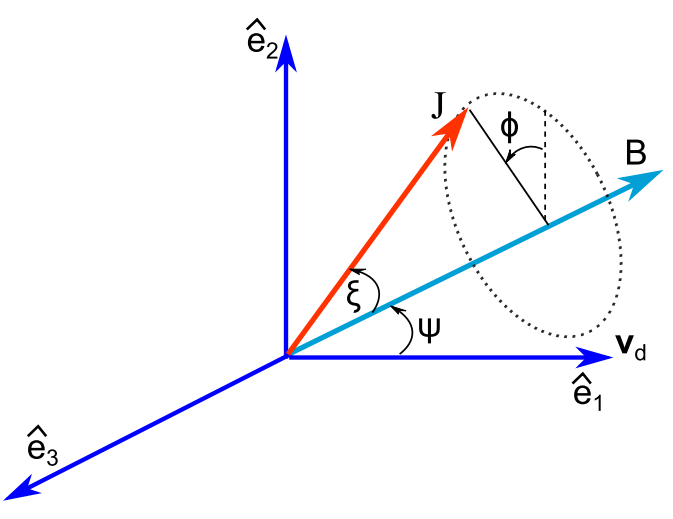


Figure 4. Alignment coordinate system $\hat{e}_1\hat{e}_2\hat{e}_3$. The axis \hat{e}_1 is chosen to be parallel to v_d , the magnetic field lies in $\hat{e}_1\hat{e}_2$ and makes an angle ψ with respect to v_d . The orientation of J is described by ξ and ϕ .

where $V=4\pi a_{\rm eff}^3/3$ is the grain volume, $\hat{B}=B/5\mu{\rm G}$ is the normalized magnetic field strength, and $\hat{K}=K(\omega)/10^{-13}\,{\rm s}$ and $K(\omega)=\chi_2(\omega)/\omega$ with $\chi_2(\omega)$ is the imaginary part of complex magnetic susceptibility of the grain material (see Hoang & Lazarian 2016).

5.2. Equation of Steady Motion

For convenience, we assume that the magnetic field is in the plane $\hat{e}_1\hat{e}_2$ and makes an angle ψ with \hat{e}_1 (also the grain drift direction v_d ; see Figure 2).

To capture the essence of MAT alignment, we assume that the axis of maximum inertia moment \hat{a}_1 is coupled to the angular momentum (DW97; LH07a). The effect of thermal fluctuations within the grain that induces the fluctuations of \hat{a}_1 with J (Lazarian & Roberge 1997) is disregarded. We also disregard the stochastic effect by gas random collisions (Hoang & Lazarian 2008) and consider the steady rotation dynamics.

MAT alignment of grains is studied by following the evolution of the grain angular momentum subject to MATs, gas damping torque, and magnetic torque. The equation of motion is then described by

$$\frac{d\mathbf{J}}{dt} = \Gamma_{\text{MAT}} + \Gamma_{\text{gas}} + \Gamma_{m},\tag{18}$$

where Γ_m is the magnetic damping torque due to paramagnetic relaxation. Here we also disregard the damping due to infrared emission, which is subdominant for large grains (Hoang et al. 2010).

To study the alignment of the grain angular momentum with respect to the magnetic field, we use the spherical coordinate system (J, ξ, ϕ) (see Figure 4). In this coordinate system, $\Gamma_m = -(\hat{\xi} \sin \xi \cos \xi + \hat{a}_1 \sin \xi^2) I_1 \omega / \tau_m$. Thus, the equations of motion for these variables become

$$\frac{dJ}{dt} = \pi a_{\text{eff}}^3 n_{\text{H}} m_{\text{H}} v_{\text{th}}^2 H - \frac{J}{\tau_{\text{gas}}} - \frac{\sin^2 \xi}{\tau_m}$$
 (19)

$$\frac{d\xi}{dt} = \frac{\pi a_{\text{eff}}^3 n_{\text{H}} m_{\text{H}} v_{\text{th}}^2}{J} F - \frac{\sin \xi \cos \xi}{\tau_m},\tag{20}$$

$$\frac{\sin \xi d\phi}{dt} = \frac{\pi a_{\text{eff}}^3 n_{\text{H}} m_{\text{H}} v_{\text{th}}^2}{J} G - \frac{2\pi}{\tau_{\text{Lar}}},\tag{21}$$

where F, H, and G are the aligning, spin-up and precessing torque components of MATs, which are the functions of the angles ξ , ψ , ϕ (see the Appendix), and τ_{Lar} is the Larmor precession timescale around the magnetic field.

The Larmor precession is usually fast compared to the main dynamical timescales, except in the very dense conditions such as protoplanetary disks (Hoang & Lazarian 2016). Thus, the averaging over ϕ angle is carried out to simplify the equations of motion. As a result, the equations of motion for $J'=J/I_1\omega_T$ and $t'=t/\tau_{\rm gas}$ become

$$\frac{d\xi}{dt'} = \frac{M\langle F(\xi, \psi)\rangle}{J'} - \delta_m \sin \xi \cos \xi, \tag{22}$$

$$\frac{dJ'}{dt'} = M \langle H(\xi, \psi) \rangle - J'(1 + \delta_m \sin^2 \xi), \tag{23}$$

where $\omega_T = (2kT_{\rm gas}/I_1)^{1/2}$, $\langle F(\xi, \psi) \rangle$, and $\langle H(\xi, \psi) \rangle$ are aligning and spin-up torque components averaged over the Larmor precession (see the Appendix), and

$$M = \frac{n_{\rm H} m_{\rm H} v_{\rm th}^2 \pi a_{\rm eff}^3 \tau_{\rm gas}}{I_1 \omega_T}.$$
 (24)

For the following calculations, we consider MATs from the multiple scattering regime, and the physical parameters for the cold neutral medium (CNM; $n_{\rm H}=30~{\rm cm}^{-3}$, $T_{\rm gas}=100~{\rm K}$) are adopted.

Figure 5 shows the spin-up $\langle H \rangle$ and aligning $\langle F \rangle$ torque components for the different shapes when the drift velocity is parallel to the ambient magnetic field. Shapes 3 and 5 have similar forms of $\langle F \rangle$ and $\langle H \rangle$, where zeros of $\langle F \rangle$ (i.e., stationary points) occur at $\sin \Theta = 0$.

5.3. Suprathermal Rotation by MATs

To see whether MATs can spin up grains to suprathermal rotation, we calculate the angular momentum at the stationary point $\sin \xi = 0$, as follows (see Equation (23)):

$$\frac{J_{\text{max}}^{\text{MAT}}(\psi)}{I_1 \omega_T} = M \langle H(\xi = 0, \psi) \rangle, \tag{25}$$

which corresponds to the maximum angular momentum spunup by MATs when J is parallel to the magnetic field. We compute J_{\max}^{MAT} for the different grain sizes and the drift direction ψ .

Figure 6 (left panel) shows $J_{\rm max}^{\rm MAT}$ as a function of the grain size for the different grain shapes and $s_d=1$. Results predicted by AMO, where its magnitude is multiplied by a factor of 2×10^{-4} is also shown by a red solid line for comparison. Since the MAT efficiency is linearly proportional to s_d , the value of $J_{\rm max}^{\rm MAT}$ for an arbitrary s_d is easily evaluated. The value of $J_{\rm max}^{\rm MAT}$ varies significantly with the grain shape, with largest torques for shape 7 and smallest torques for shape 1 of mirror symmetry as expected. The value of $J_{\rm max}^{\rm MAT}$ scales as $a_{\rm eff}$.

Figure 6 (right panel) shows the value of $J_{\rm max}^{\rm MAT}$ as a function of ψ for the different shapes and two typical grain sizes. For shapes 6 and 7, $J_{\rm max}^{\rm MAT}$ tends to decrease with increasing ψ and reach minimum at $\psi=90^{\circ}$. In contrast, for shapes 2–5, $J_{\rm max}^{\rm MAT}$ is minimum at $\psi=0^{\circ}$ and tends to increase with increasing ψ

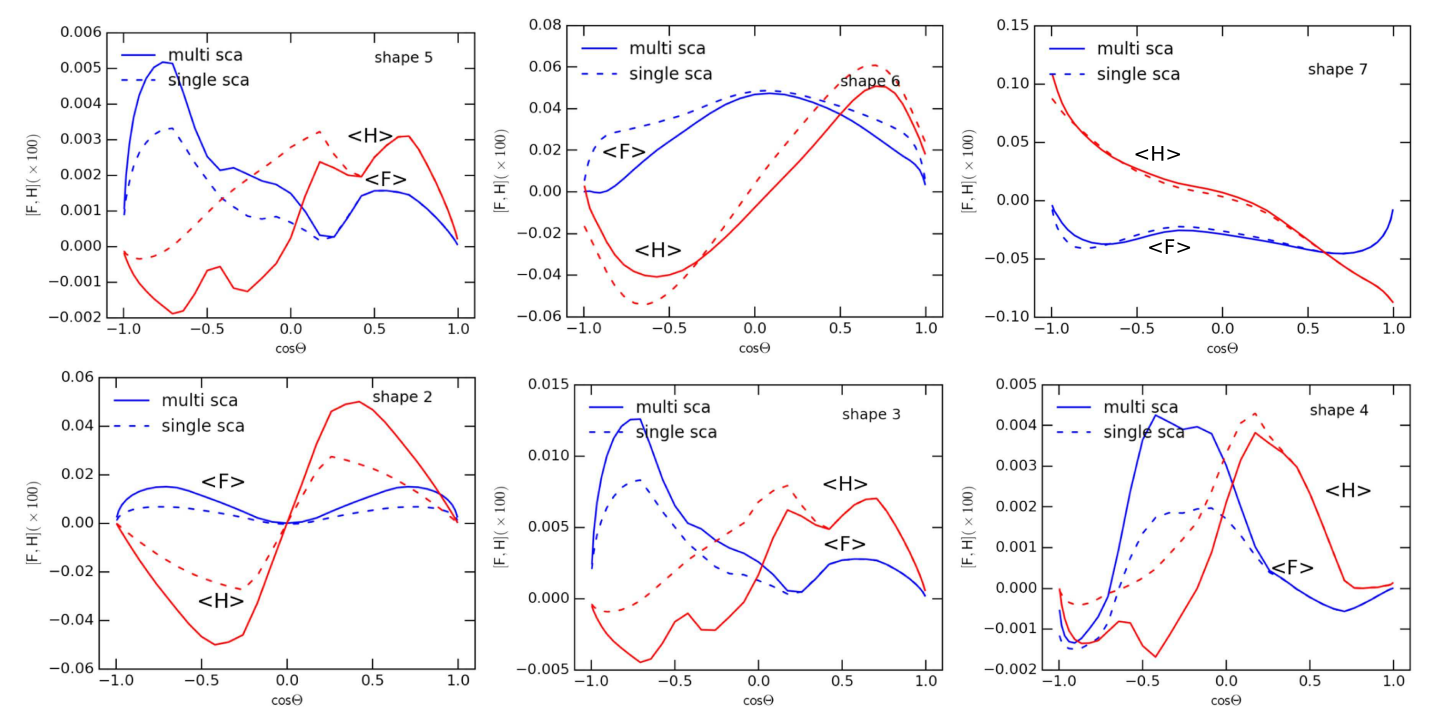


Figure 5. Spin-up and aligning torque components for $\psi = 0^{\circ}$. Both single scattering (solid lines) and multiple scattering (dashed lines) are considered. The different shapes are shown.

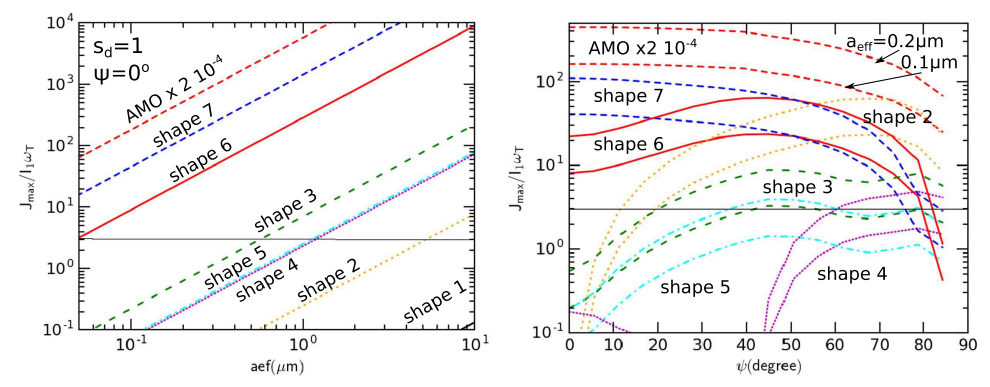


Figure 6. Left panel: maximum angular momentum J_{\max} spun-up by MATs from AMO and irregular grains vs. grain size for the drift angle $\psi=0^{\circ}$. Right panel: J_{\max} vs. ψ computed for $a_{\text{eff}}=0.1$ and $0.2~\mu\text{m}$. The horizontal line marks the suprathermal rotation limit of $3I_1\omega_T$. The results for $s_d=1$ are shown.

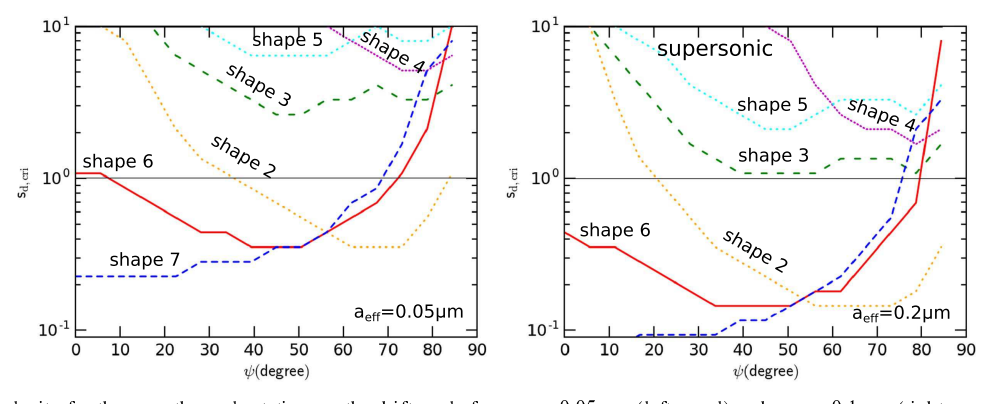


Figure 7. Critical drift velocity for the suprathermal rotation vs. the drift angle for $a_{\rm eff}=0.05~\mu{\rm m}$ (left panel) and $a_{\rm eff}=0.1~\mu{\rm m}$ (right panel). Grains of shapes 2, 6, and 7 can be suprathermal rotation at subsonic drift, i.e., $s_d<1$, while shapes 3–5 require supersonic drift to reach suprathermal rotation.

up to $\psi \sim 50^\circ$. Thus, shapes 2–5 can still be driven to suprathermal rotation for large drift angles (see Figure 6).

To derive the critical value of the drift velocity, $s_{d,cri}$, that a given grain can be driven to suprathermal rotation by MATs, we

compute $J_{\text{max}}^{\text{MAT}}$ for a wide range of s_d and grain sizes. Figure 7 shows the obtained value $s_{d,\text{cri}}$ as a function of the drift angle for the two values of a_{eff} . Grains of HIS (shapes 2, 6, and 7) can be driven to suprathermal rotation even with subsonic velocity of

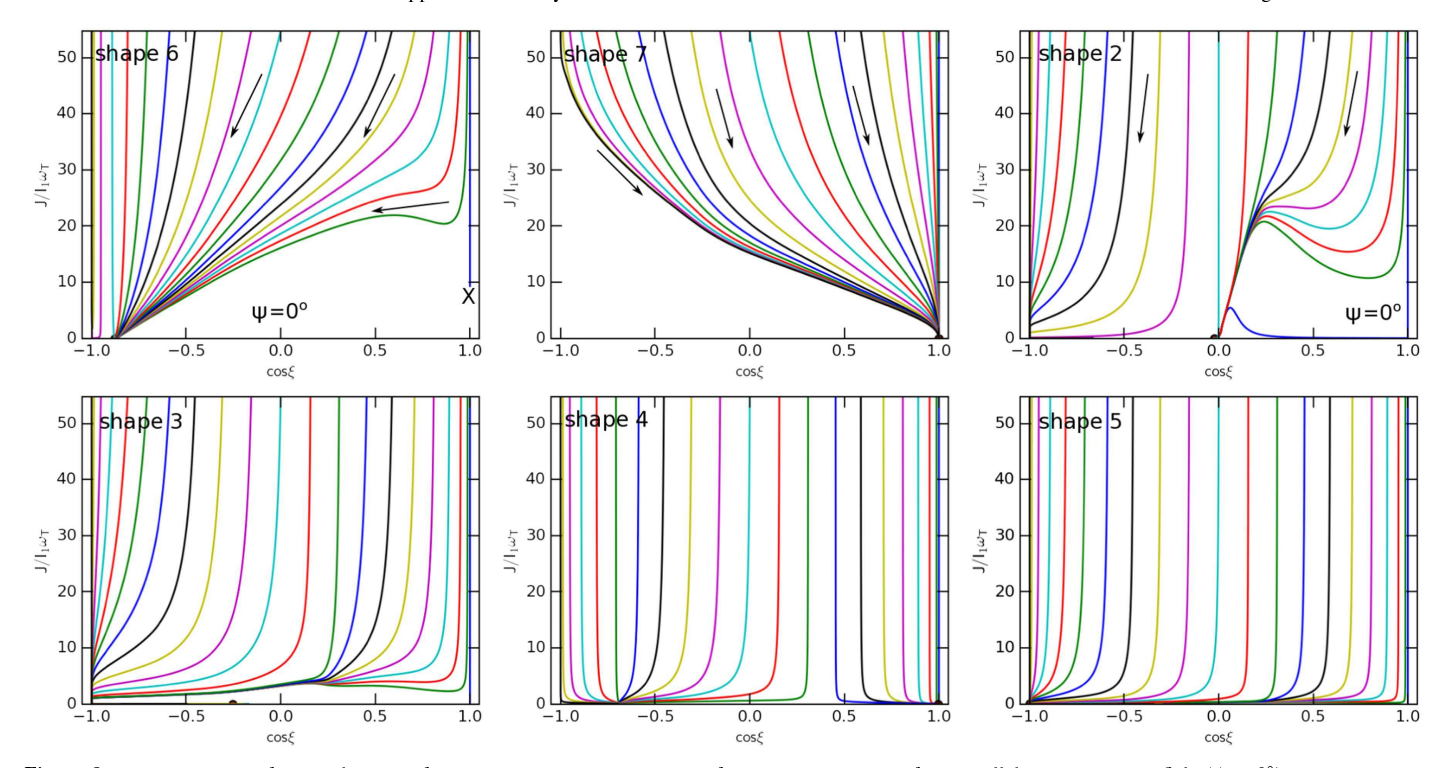


Figure 8. Trajectory maps of MAT alignment for ordinary paramagnetic grains of the various shapes drifting parallel to the magnetic field ($\psi = 0^{\circ}$). Arrows indicate the change of the grain orientation over time. Two repellor points (marked by X) are seen for shapes 6 and 7, and grains are driven to low-J attractor points.

 $s_d \sim 0.1$. In contrast, grains of WIS (shapes 3–5) only achieve suprathermal rotation when grains are moving at supersonic speeds ($s_d \ge 1$).

5.4. Phase Trajectory Map of MAT Alignment

In the following, we will study the trajectory phase map of these shapes. The instantaneous orientation of the grain in the lab frame \hat{e}_i for i = 1, 2, 3 can be characterized by J and ξ . To study MAT alignment, we first solve Equations (22) and (23) numerically with timestep $dt' = \min[10^{-3}, 0.1/\delta_m]$, where $t'=t/\tau_{\rm gas}$ and $\delta_m=\tau_{\rm gas}/\tau_m$. There, we visualize MAT alignment in terms of phase trajectory map J(t), $\xi(t)$. We consider an ensemble of grains with the different initial orientations ξ drawn from a uniform distribution and $J = J_0$. We assume that the axis \hat{a}_1 is parallel to **J** and shows the results for this positive flipping state. Grains may be in the negative flipping state of \hat{a}_1 antiparallel to J. However, when the thermal flipping is taken into account, the trajectory maps of the two flipping states are identical (Hoang & Lazarian 2008; Hoang & Lazarian 2009b), thus we show the maps for the positive flipping case only. Shape 1 has very small MATs, thus, it is not of interest to study the trajectory map for this shape.

5.4.1. Ordinary Paramagnetic Grains

We first study alignment for ordinary paramagnetic grains. Figure 8 shows trajectory maps for the different shapes and $\psi=0^\circ$. Grains are driven to low-J attractors, and only shapes 6 and 7 have the high-J repellors (denoted by the cross). For most of the shapes, the low-J attractors occur at $\cos\xi\approx\pm1$. Due to the low MATs, the orientation of grains of shapes 3–5 are hardly changed for $J>I_1\omega_T$.

Grain alignment at low-J attractors is unstable because of the low angular momentum (Hoang & Lazarian 2008). When stochastic excitations by gas collisions are taken into account, grains aligned at the low-J attractors will be disturbed substantially. Thus, the degree of MAT alignment is low in the absence of high-J attractors (Hoang & Lazarian 2016).

5.4.2. Superparamagnetic Grains with Iron Inclusions

Next, we investigate the MAT alignment for superparamagnetic grains containing iron inclusions. Although a large value of δ_m up to 100 can be achieved when grains contain big iron clusters, the essential effect is not much different due to the saturation of grain alignment (Hoang & Lazarian 2016). Thus, we show the results for a typical value of $\delta_m = 2$.

Figure 9 shows the phase trajectory maps for superparamagnetic grains at $\psi=0^\circ$. The high-J repellor point in shapes 2, 6, and 7 is converted to an attractor point due to the superparamagnetic effect. Due to opposite helicity, the attractor point in shape 7 occurs at $\cos\xi=-1$, corresponding the the angular momentum antiparallel to ${\bf B}$. Other shapes have only low-J attractors. We also run simulations for $\delta_m=10$ and find that the trajectory maps are similar to those with $\delta_m=2$, except the fraction of grains driven to high-J attractors is increased.

While accounting for stochastic excitation by gas collisions, grains are eventually driven to the high-*J* attractors (Hoang & Lazarian 2016), leading to perfect alignment. Therefore, the degree of MAT alignment of shapes 2, 6, and 7 is expected to be perfect thanks to the presence of high-*J* attractors, while shapes 1, 3–5 are weakly aligned due to the absence of high-*J* attractors.

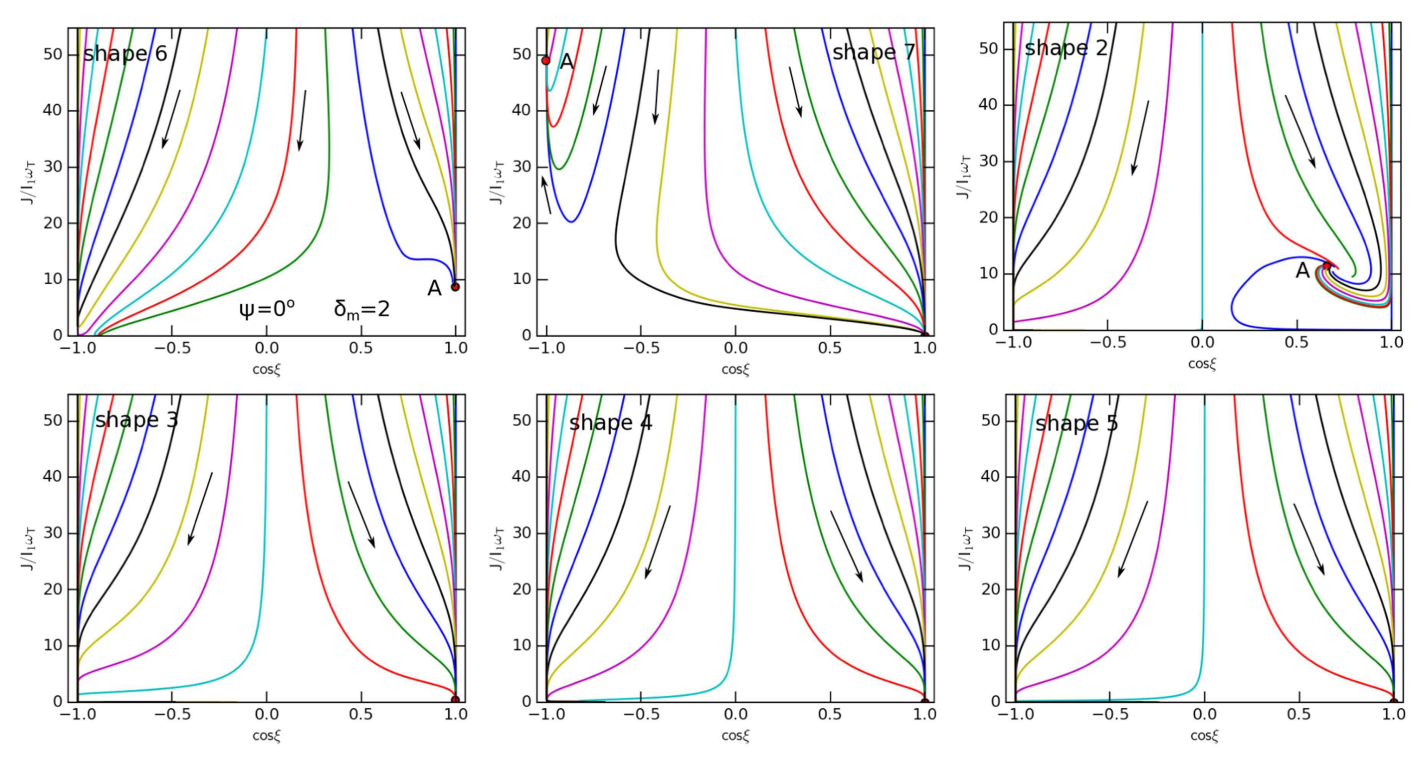


Figure 9. Same as Figure 8, but for superparamagnetic grains with $\delta_m = 2$. Shapes 2, 6, and 7 have high-*J* attractor points (denoted by a filled circle, point A) due to enhanced magnetic relaxation and MATs, while other shapes exhibit only low-*J* attractor points.

5.5. Dependence of MAT Alignment on the Drift Direction

To see the dependence of MAT alignment on the drift direction with respect to the ambient magnetic field, we solve equations of motion for the trajectory map for several angles $\psi = 30^{\circ}$, 60° , 80° .

Figure 10 shows the trajectory maps for the case of ordinary paramagnetic grains of shapes 2, 6, and 7. For shape 6, MAT alignment has only low-J attractors (with high-J repellor points). The high-J attractor is present for $\psi=60^\circ$ in the trajectory map of shape 7. For shape 2, MAT alignment can occur with high-J attractors (filled circles) for the $\psi=60^\circ$ and 80° .

Similarly, Figure 11 shows the results for superparamagnetic grains. For three HIS (shapes 2, 6, and 7), the high-J attractors appear for all angles ψ . Therefore, MAT alignment for superparamagnetic grains can achieve perfect alignment when random collisional excitations are accounted for. For other WIS (shapes 3–5), we expect the effect of iron inclusions is negligible for small drift angles (i.e., $\psi < 30^{\circ}$) because MATs are insufficient to produce suprathermal rotation, such that the superparamagnetic torque can stabilize its alignment (see Figure 6). For large drift angles, iron inclusions can induce perfect alignment as shapes 2, 6, and 7.

6. Discussion

6.1. MAT Efficiency of Irregular Grains and Comparison with Lazarian & Hoang's (2007b) Analytical Model

First, MATs of irregular grains introduced in LH07b are very different from the torques that act in the original mechanism (Gold 1952b) as well as in alternative mechanical alignment mechanisms proposed in the last century, e.g., from the cross-sectional and crossover mechanical alignment suggested in Lazarian (1995b). The MATs from LH07b act analogously to

radiative torques by increasing the angular momentum of a grain in proportion of time. This makes them radically different from the Gold stochastic torques. The latter act on regular oblate or prolate grains, but grain irregularities render grains with helicity in terms of their interaction with the gaseous flow. This helicity induces the new type of torque and alignment.

We find that the grain shape that exhibits mirror symmetry produces negligible MATs. Interestingly, for HIS, including shapes 2, 6, and 7, we find that MATs are strong and able to drive grains to suprathermal rotation with subsonic drift. Moreover, MATs of these shapes also exhibit generic properties as predicted by the AMO, including symmetric Q_{e1} and zeros of Q_{e2} when the drift direction is parallel to the axis of maximum moment of inertia \hat{a}_1 . For WIS (shapes 3–5), the magnitude of MATs is found to be lower. Our numerical results demonstrate the role of the grain surface properties on MATs.

In LH07b, we discussed two possibilities that can reduce MATs from our AMO, including the reflection coefficient E and degree of helicity D. In that sense, the AMO can be considered to have perfect helicity, i.e., D=1. Naturally, most of the grains do not have clear-cut facets as the grain model of LH07b, but have numerous irregularities, which can be considered of numerous facets of different orientations, leading to the reduction of helicity D.

For a simple shape considered in Section 2.2, we have shown that the MAT efficiency decreases with increasing the number of facets N_{facet} . We note that the random walk formula adopted for our analytical estimates is applicable only for $N_{\text{facet}} \gg 1$, i.e., not applicable for shapes 3–5 with a few facets.

We can then quantify the degree of helicity of an arbitrary irregular shape as follows:

$$D \equiv \frac{\max(J_{\max}^{\text{irr}}(\psi))}{\max(J_{\max}^{\text{AMO}}(\psi))},\tag{26}$$

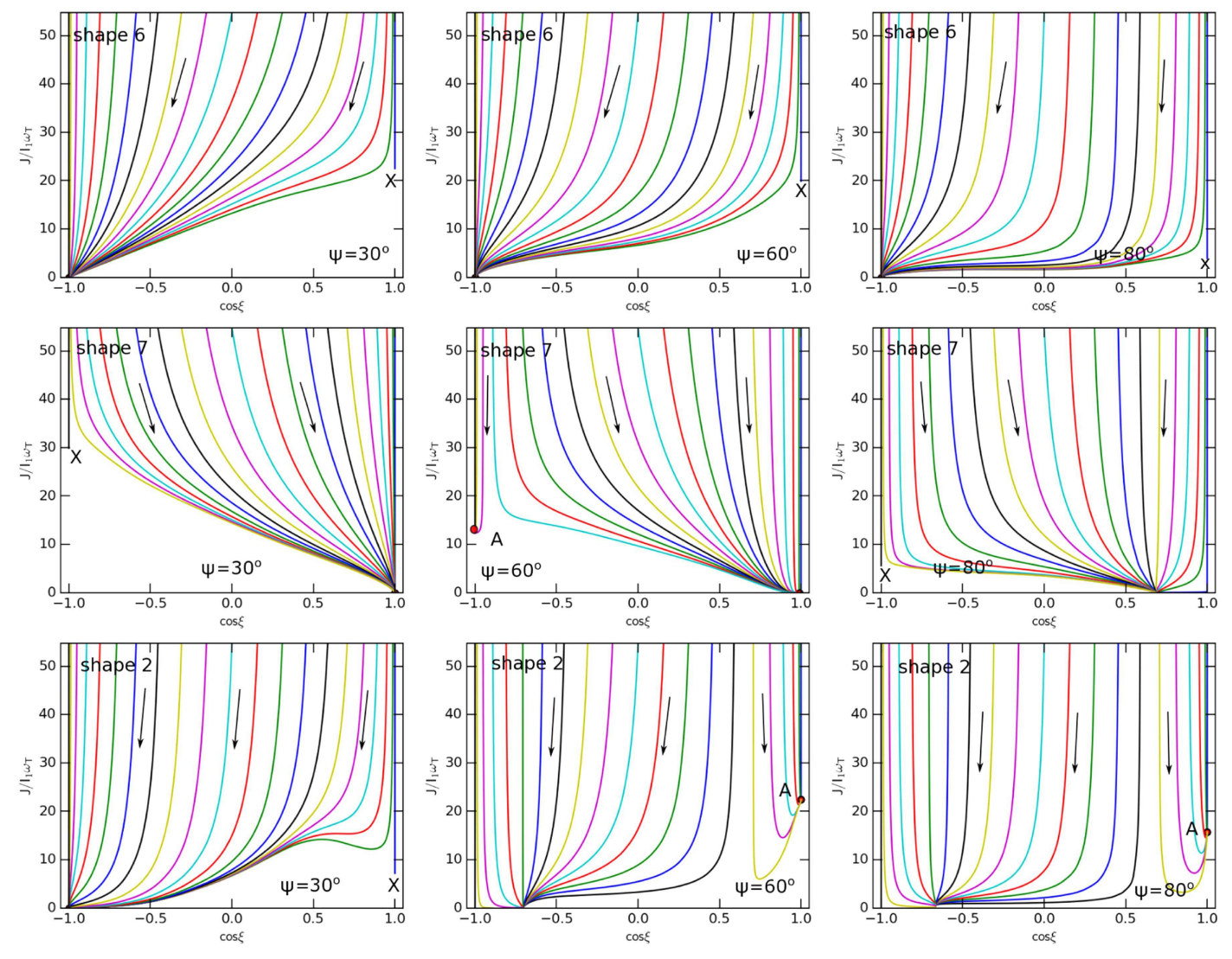


Figure 10. Phase maps for the different angles $\psi = 30^{\circ}$, 60° , 80° for shape 6 (top panels), shape 7 (middle panels), and shape 2 (bottom panels). Shape 2 has high-*J* attractor points, while shape 6 has only low-*J* attractor points. The drift speed of $s_d = 1$ is considered.

where $J_{\max}^{irr}(\psi)$ and $J_{\max}^{AMO}(\psi)$ are the maximum spin-up momentum evaluated with MATs from irregular shapes and AMO, respectively. The obtained value D for the selected shapes is shown in Table 8. HIS have larger values D than WIS, and the symmetry shape 1 has a negligible degree of helicity as expected.

6.2. MAT Alignment and Comparison to RAT Alignment

We note that shapes 6 and 7 were created to calculate RATs, and they found strong RATs for these shapes. Interestingly, we found that MATs for these shapes are also strong and exhibit the same helicity (right helicity for shape 6 and left helicity for shape 7) and generic properties as RATs. We also find that our new shape 2 can produce strong MATs, comparable to those of shapes 6 and 7.

For HIS grains, we find that subsonic drift can spin-up the typical 0.1 μ m grains to suprathermal rotation. For such grain shapes, MAT alignment exhibits low-J and high-J repellor/attractor points in the phase trajectory map and has a long axis perpendicular to the magnetic field, which is analogous to RAT alignment. In the presence of iron inclusions, repellor points are

converted to high-*J* attractors due to the enhanced magnetic relaxation. For WIS grains (shapes 3–5), supersonic drift is required to achieve suprathermal rotation. Thus, in the typical ISM conditions, all grains are driven to thermal rotation by gas damping.

MAT alignment also depends on the drift direction. For shapes 6 and 7, we find that the grain maximum angular momentum spun-up by MATs, $J_{\rm max}^{\rm MAT}$, tends to decrease with the angle ψ . However, MAT alignment of shapes 2–5 tends to increase with ψ and become flat (see Figure 6).

Table 8 compares the MAT and RAT alignment for seven irregular shapes, where RH and LH denote right helicity and left helicity. Both MAT alignment and RAT alignment with low-J/high-J attractors and repellors are indicated. The presence of high-J attractors for shape 3 is only achieved at some large drift angles (see Figure 6).

Numerous observations of dust polarization show the correspondence to the predictions by RAT alignment for molecular clouds (Whittet et al. 2008; Andersson et al. 2011) and starless cores (Alves et al. 2014; Jones et al. 2015). This reveals that MAT alignment is not a dominant mechanism in these environments. Therefore, for the CMB polarization

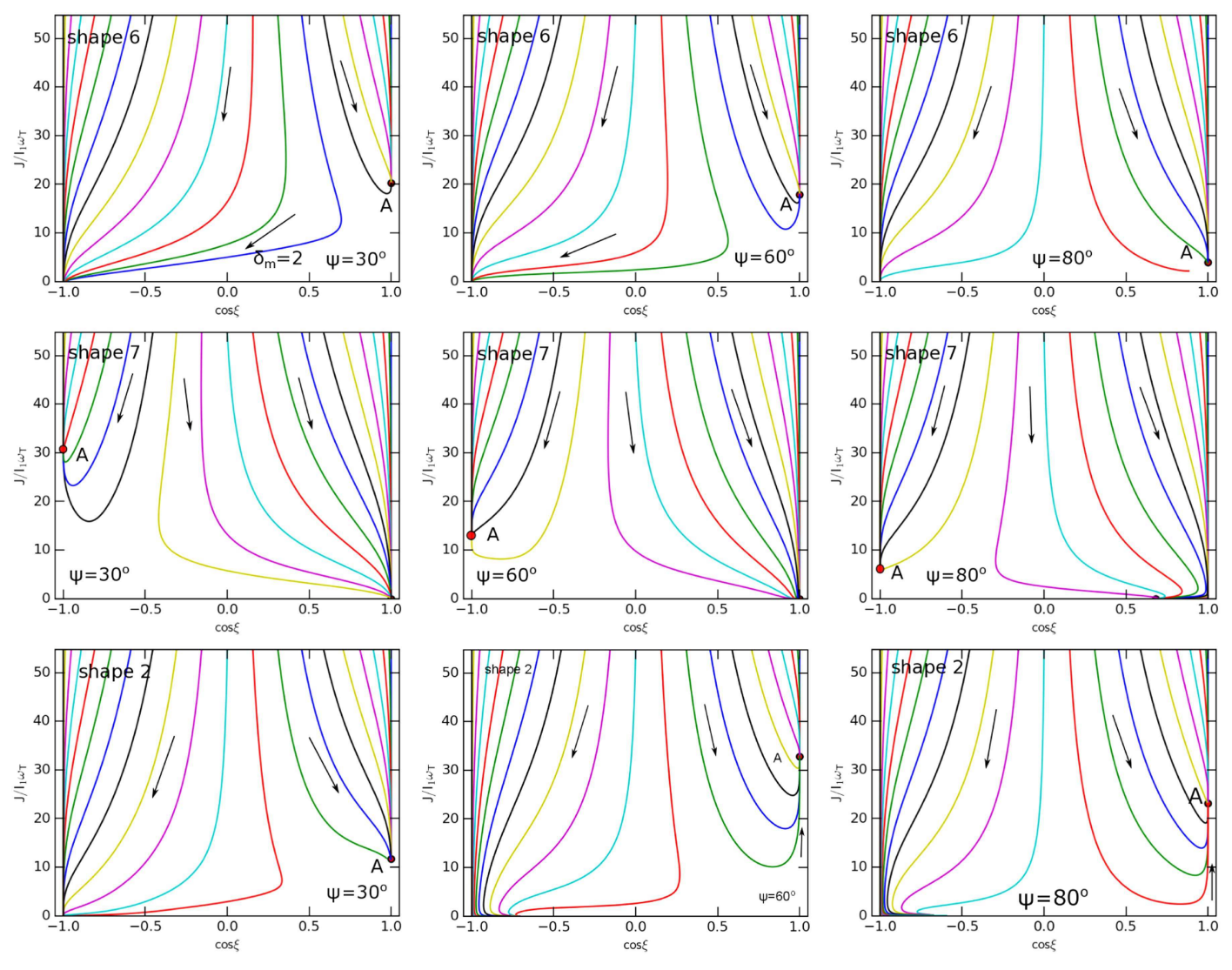


Figure 11. Same as Figure 10, but for superparamagnetic grains with $\delta_m = 2$. Grains are perfectly aligned at high-J attractor points and low-J attractor points.

Table 8 Characteristics of MAT Alignment vs. RAT Alignment for the $a_{\rm eff}=0.1~\mu{\rm m}$ Grains in the Typical ISM Conditions and $s_d\sim 1$

Shape	Helicity	MATs	D	MAT Align	SMAT Align	Helicity	RATs	RAT Align	SRAT Align
1	Sym	negligible	1.3×10^{-10}	NA	NA	NA			
2	RH	strong	2.5×10^{-5}	high- J rep./attr.	high-J attr.	NA		•••	•••
3	RH	moderate	3.6×10^{-6}	high- J rep./attr.	high-J attr.	NA		•••	•••
4	RH	moderate	1.9×10^{-6}	low- J rep./attr.	low-J attr.	NA		•••	•••
5	RH	moderate	1.6×10^{-6}	low- J rep./attr.	low-J attr.	NA		•••	•••
6	RH	strong	2.6×10^{-5}	high- J rep./attr.	high-J attr	RH	strong	high-Jrep./attr.	high-J attr.
7	LH	strong	4.5×10^{-5}	high- J rep./attr.	high-J attr.	LH	strong	high-Jrep./attr.	high-J attr.

studies, which are involved in the diffuse ISM, the modeling of foreground polarization is not going to be further complicated by the presence of MAT alignment due to the dominance of RAT alignment.

6.3. Astrophysical Environments with Potential MAT Alignment

We now discuss the potential environment conditions where MAT alignment is important. In general, dust-gas drift can be triggered by cloud-cloud collisions (Gold 1952b), radiation

pressure, ambipolar diffusion, and gravitational sedimentation (see Lazarian 2007).

First, interstellar cloud–cloud collisions are usually triggered by strong radiation pressure from supernova explosions, producing supersonically drifting grains. Thus, MAT alignment is expected to be efficient in such clouds. The line of sight to SN 2014J is thought to encounter numerous individual clouds (Patat et al. 2015). Therefore, observations of polarization toward SNe Ia can provide useful tests for MAT alignment (Hoang 2017).

Second, in outflows around the late-type stars (e.g., Asymptotic Giant Branch (AGB), post-AGBs, and planetary nebulae (PNe)), grains are found to be supersonically drifting through the gas due to strong radiation pressure (see Netzer & Elitzur 1993). Thus, we expect MAT alignment to be important in these conditions. Grains are also expected to drift in the innermost outflow regions around high-mass young stellar objects where the outflow is produced by radiation pressure instead of hydromagnetic effects.

Third, Roberge et al. (1995) found that for supersonically drifting grains in a weakly magnetized molecular cloud by ambipolar diffusion, Gold alignment can produce the alignment efficiency of $R \sim 0.3$ for $s_d \gg 1$ and $\delta_m = 10$ (i.e., superparamagnetic grains). Our results show that for grains of HIS, MAT alignment can be efficient, and superparamagnetic grains can be perfectly aligned. This unique feature allows us to differentiate classical Gold alignment from MAT alignment.

Recently, fast modes of MHD turbulence are found to accelerate charged dust grains to supersonic speeds (Yan & Lazarian 2003; Yan et al. 2004; Hoang et al. 2012). Moreover, transit time damping is found to be an efficient acceleration mechanism (Hoang et al. 2012). For the CNM, the MHD turbulence can produce the drift speed of $v_d \sim 1.5 \, \mathrm{km \, s^{-1}}$, corresponding to $s_d \sim 1.2$. In molecular and dark clouds, Yan et al. (2004) obtained $s_d \sim 1.1-2.2$ and $\sim 2.7-3.5$ for $a=0.1-1.0 \, \mu \text{m}$. Compared to the critical drift speed for MAT alignment in Figure 7, we see that the MAT alignment is important in dark clouds for the drift angles of $\psi > 20^{\circ}$ with the magnetic field. Interestingly, it is found that MHD turbulence tends to accelerate grains in the direction that makes a large angle with the mean magnetic field (Yan et al. 2004). In protoplanetary disks where MRI activity is active, turbulence is perhaps sufficient to generate drift motion of grains and trigger MAT alignment by superparamagnetic grains.

Other processes, such as photoelectric force due to the ejection of photoelectrons by anisotropic radiation, photodesorption of atoms, can also induce relative motion of grains with the ambient gas. However, these processes are unable to drive grains to supersonic motion (Weingartner & Draine 2001).

Gold mechanical alignment was referred to explain polarization observed in outflows around protostars, i.e., early stages of star formation (Rao et al. 1998; Cortes et al. 2006; Tang et al. 2009). In light of the new MAT mechanism, we expect the efficient alignment of HIS grains with the magnetic fields by MATs in outflows. The MAT alignment mechanism helps to probe magnetic fields in special conditions where radiative alignment fails due to the lack of a radiation source.

6.4. Effect of Grain Precession around the Drift Direction versus Larmor Precession

For grains in the interstellar diffuse medium, the Larmor precession of the grain magnetic moment around the ambient magnetic field is usually fast due to the large magnetic moments rendered by grains as a result of the Barnett effect (Dolginov & Mitrofanov 1976; see also Lazarian et al. 2015). Grains are aligned with the magnetic fields. There are special situations when the axis of alignment is not the magnetic field but the direction of the grain drift. Physically, this means that the grain precession induced by the gaseous bombardment is faster than the Larmor precession. This is shown to occur for

ordinary grains in the protoplanetary disks with very high density, in which the Larmor precession is slower than the gas damping. In these conditions, if the grain drift is supersonic, the alignment can occur with the drift direction due to the MAT. If this is the case, then it can allow us to trace the direction of outflows using the polarization mapping.

6.5. MAT Alignment in the Presence of Pinwheel Torques, Strong and Weak Internal Relaxation

Finally, let us discuss MAT alignment of grains in the presence of pinwheel torques and alignment of grains without internal relaxation.

Purcell (1979) suggested several processes that can spin-up grains to suprathermal rotation, including formation of hydrogen molecules on the grain surface, the variation of accommodation coefficient and emissivity on the grain surface. Although for small grains the effect of pinwheel torques is suppressed due to rapidly flipping and thermal trapping (Lazarian & Draine 1999), for large grains, it is still effective. Hoang & Lazarian (2009b) found that RAT alignment is shown to be enhanced by pinwheel torques. The effect of alignment by H₂ torques is observed in reflection nebula IC 63 (Andersson et al. 2013), and it is successfully modeled by Hoang et al. (2015). Since MAT alignment of irregular shapes is essentially similar to RAT alignment, we predict that pinwheel torques also act to enhance the alignment by lifting the low-*J* attractor points and create new high-*J* attractor points.

In the presence of strong thermal fluctuations with efficient internal relaxation, we expect that the crossover becomes low-*J* attractor points. Therefore, MAT alignment occurs with low-*J* and high-*J* attractors as RAT alignment. For weak internal relaxation present in very large grains, MAT alignment is expected to be more complicated. In addition to low-*J* and high-*J* attractors, some low-*J* attractor with "wrong" alignment may be present (Hoang & Lazarian 2009a). However, due to random collisions with the gas, such a wrong low-*J* alignment will be reduced, leading to a moderate degree of alignment.

7. Summary

We have studied the alignment of grains by mechanical torques for seven different irregular shapes. Our results are summarized as follows:

- 1. Among seven considered shapes, shape 1 induces negligible mechanical torques due to its mirror symmetry. HIS (shapes 2, 6, and 7) can produce strong mechanical torques that exhibit some generic properties as seen in RATs. Weakly irregular shapes (WIS, shapes 3–5) produce smaller mechanical torques. Such a dramatic difference in MATs for the considered shapes is expected from the physics of mechanical torques that only depends on the grain surface.
- 2. HIS grains can be driven to suprathermal rotation with subsonic drift, while WIS grains are only driven to suprathermal rotation with supersonic drift. The suprathermal rotation rate is found to depend on the drift angle and the grain shape.
- 3. For three HIS, we find that MAT tends to align grains with low-*J* attractors and high-*J* repellors/attractors. MAT alignment appears to depend on the grain drift direction about the magnetic field.

- 4. We find that superparamagnetic inclusions in HIS grains can help MAT alignment to align with high-*J* attractor points, producing a high degree of grain alignment. For supersonic drift, we also find that irregular grains can be perfectly aligned by MATs, while the Gold classical mechanism only induces imperfect alignment.
- 5. Our numerical results demonstrate the importance of MAT alignment and its dependence on the grain surface irregularity. Due to the uncertainty of grain shapes in the ISM, the efficiency of MAT alignment requires further theoretical and observational studies.

We thank Stefan Reissl for useful comments. T.H. acknowledges the support by the Basic Science Research Program through the National Research Foundation of Korea (NRF), funded by the Ministry of Education (2017R1D1A1B03035359). J.C.'s work is supported by the National R&D Program funded by the Ministry of Education (NRF-2016R1D1A1B02015014). A.L. acknowledges the financial support from NASA grant NNX11AD32G, NSF grant AST 1109295, and NASA grant NNH 08ZDA0090.

Appendix Aligning, Spin-up, and Precessing Torque Components

In the alignment coordinate system $\hat{e}_1\hat{e}_2\hat{e}_3$, the MAT components that cause spin-up, precession, and alignment of grains, are given by

$$F(\xi, \psi, \phi) = Q_{e1}(-\sin\psi\cos\xi\cos\phi - \sin\xi\cos\psi) + Q_{e2}(\cos\psi\cos\xi\cos\phi - \sin\xi\sin\psi) + Q_{e3}\cos\xi\sin\phi,$$

$$(27)$$

$$G(\xi, \psi, \phi) = Q_{e1}\sin\psi\sin\phi - Q_{e2}\cos\psi\sin\phi + Q_{e3}\cos\phi,$$

$$(28)$$

$$H(\xi, \psi, \phi) = Q_{e1}(\cos \psi \cos \xi - \sin \psi \sin \xi \cos \phi) + Q_{e2}(\sin \psi \cos \xi + \cos \psi \sin \xi \cos \phi) + Q_{e3} \sin \xi \sin \phi,$$
(29)

where $Q_{e1}(\xi, \psi, \phi)$, $Q_{e2}(\xi, \psi, \phi)$, $Q_{e3}(\xi, \psi, \phi)$, as functions of ξ , ψ , and ϕ , are components of the RAT efficiency vector in the lab coordinate system (see DW97; LH07a).

To obtain $Q_{e1}(\xi, \psi, \phi)$, $Q_{e2}(\xi, \psi, \phi)$, and $Q_{e3}(\xi, \psi, \phi)$ from $Q_{\Gamma}(\Theta, \beta, \Phi)$, we need to use the relations between ξ, ψ, ϕ and Θ, β, Φ (see Weingartner & Draine 2003; HL08).

The average of the aligning torque over the Larmor precession is given by

$$\langle F(\xi, \psi) \rangle = \frac{1}{2\pi} \int_0^{2\pi} F(\xi, \psi, \phi) d\phi. \tag{30}$$

ORCID iDs

Thiem Hoang https://orcid.org/0000-0003-2017-0982 Jungyeon Cho https://orcid.org/0000-0003-1725-4376

References

```
Ade, P. A. R., Aghanim, N., Ahmed, Z., et al. 2015, PRL, 114, 101301
Alves, F. O., Frau, P., Girart, J. M., et al. 2014, A&A, 569, L1
Andersson, B.-G., Lazarian, A., & Vaillancourt, J. E. 2015, ARA&A, 53, 501
Andersson, B.-G., Piirola, V., De Buizer, J., et al. 2013, ApJ, 775, 84
Andersson, B.-G., Pintado, O., Potter, S. B., Straižys, V., & Charcos-Llorens, M.
   2011, A&A, 534, 19
Chandrasekhar, S., & Fermi, E. 1953, ApJ, 118, 113
Cho, J., & Lazarian, A. 2005, ApJ, 631, 361
Cho, J., & Lazarian, A. 2007, ApJ, 669, 1085
Cortes, P. C., Crutcher, R. M., & Matthews, B. C. 2006, ApJ, 650, 246
Das, I., & Weingartner, J. C. 2016, MNRAS, 457, 1958
Davis, L. 1951, PhRv, 81, 890
Davis, L. J., & Greenstein, J. L. 1951, ApJ, 114, 206
Dolginov, A. Z., & Mitrofanov, I. G. 1976, Ap&SS, 43, 291
Draine, B. T., & Weingartner, J. C. 1996, ApJ, 470, 551
Draine, B. T., & Weingartner, J. C. 1997, ApJ, 480, 633
Gold, T. 1952a, Natur, 169, 322
Gold, T. 1952b, MNRAS, 112, 215
Hall, J. S. 1949, Sci, 109, 166
Hildebrand, R. H. 1988, QJRAS, 29, 327
Hiltner, W. A. 1949, Sci, 109, 165
Hoang, T. 2017, ApJ, 836, 13
Hoang, T., Draine, B. T., & Lazarian, A. 2010, ApJ, 715, 1462
Hoang, T., & Lazarian, A. 2008, MNRAS, 388, 117
Hoang, T., & Lazarian, A. 2009a, ApJ, 697, 1316
Hoang, T., & Lazarian, A. 2009b, ApJ, 695, 1457
Hoang, T., & Lazarian, A. 2014, MNRAS, 438, 680
Hoang, T., & Lazarian, A. 2016, ApJ, 831, 159
Hoang, T., Lazarian, A., & Andersson, B.-G. 2015, MNRAS, 448, 1178
Hoang, T., Lazarian, A., & Schlickeiser, R. 2012, ApJ, 747, 54
Jones, T. J., Bagley, M., Krejny, M., Andersson, B.-G., & Bastien, P. 2015,
   ApJ, 149, 31
Kimura, Y., Tanaka, K. K., Nozawa, T., Takeuchi, S., & Inatomi, Y. 2017,
   SciA, 3, e1601992
Lazarian, A. 1994, MNRAS, 268, 713
Lazarian, A. 1995a, MNRAS, 277, 1235
Lazarian, A. 1995b, ApJ, 451, 660
Lazarian, A. 1997, ApJ, 483, 296
Lazarian, A. 2007, JOSRT, 106, 225
Lazarian, A., Andersson, B.-G., & Hoang, T. 2015, in Polarimetry of Stars and
  Planetary Systems, ed. L. Kolokolova, J. Hough, & A.-C. Levasseur-Regourd
  (New York: Cambridge Univ. Press), 81
Lazarian, A., & Draine, B. T. 1999, ApJL, 516, L37
Lazarian, A., & Efroimsky, M. 1996, ApJ, 466, 274
Lazarian, A., & Hoang, T. 2007a, MNRAS, 378, 910
Lazarian, A., & Hoang, T. 2007b, ApJL, 669, L77
Lazarian, A., & Hoang, T. 2008, ApJL, 676, L25
Lazarian, A., & Roberge, W. G. 1997, ApJ, 484, 230
Lazarian, A., & Yan, H. 2002, ApJL, 566, L105
Netzer, N., & Elitzur, M. 1993, ApJ, 410, 701
Patat, F., Taubenberger, S., Cox, N. L. J., et al. 2015, A&A, 577, A53
Purcell, E. M. 1969, Phy, 41, 100
Purcell, E. M. 1979, ApJ, 231, 404
Purcell, E. M., & Spitzer, L. J. 1971, ApJ, 167, 31
Rao, R., Crutcher, R. M., Plambeck, R. L., & Wright, M. C. H. 1998, ApJL,
Roberge, W. G., & Hanany, S. 1990, BAAS, 22, 862
Roberge, W. G., Hanany, S., & Messinger, D. W. 1995, ApJ, 453, 238
Tang, Y.-W., Tang, Y.-W., Ho, P. T. P., et al. 2009, ApJ, 695, 1399
Tazaki, R., Lazarian, A., & Nomura, H. 2017, ApJ, 839, 56
Weingartner, J. C., & Draine, B. T. 2001, ApJ, 553, 581
Weingartner, J. C., & Draine, B. T. 2003, ApJ, 589, 289
Whittet, D. C. B., Hough, J. H., Lazarian, A., & Hoang, T. 2008, ApJ, 674, 304
Yan, H., & Lazarian, A. 2003, ApJL, 592, L33
Yan, H., Lazarian, A., & Draine, B. T. 2004, ApJ, 616, 895
```